Metal Oxide Oxidation Catalysts as Scaffolds for Perovskite Solar Cells

Peter J. Holliman *[ID]**, Arthur Connell, Eurig W. Jones** [ID] **and Christopher P. Kershaw** [ID]

College of Engineering, Bay Campus, Swansea University, Swansea SA1 8EN, UK;
arthur.connell@swansea.ac.uk (A.C.); eurig.w.jones@swansea.ac.uk (E.W.J.); c.p.kershaw@swansea.ac.uk (C.P.K.)
* Correspondence: p.j.holliman@swansea.ac.uk

Abstract: Whilst the highest power conversion efficiency (PCE) perovskite solar cell (PSC) devices that have reported to date have been fabricated by high temperature sintering (>500 °C) of mesoporous metal oxide scaffolds, lower temperature processing is desirable for increasing the range of substrates available and also decrease the energy requirements during device manufacture. In this work, titanium dioxide (TiO_2) mesoporous scaffolds have been compared with metal oxide oxidation catalysts: cerium dioxide (CeO_2) and manganese dioxide (MnO_2). For MnO_2, to the best of our knowledge, this is the first time a low energy band gap metal oxide has been used as a scaffold in the PSC devices. Thermal gravimetric analysis (TGA) shows that organic binder removal is completed at temperatures of 350 °C and 275 °C for CeO_2 and MnO_2, respectively. By comparison, the binder removal from TiO_2 pastes requires temperatures >500 °C. $CH_3NH_3PbBr_3$ PSC devices that were fabricated while using MnO_2 pastes sintered at 550 °C show slightly improved PCE (η = 3.9%) versus mesoporous TiO_2 devices (η = 3.8%) as a result of increased open circuit voltage (V_{oc}). However, the resultant PSC devices showed no efficiency despite apparently complete binder removal during lower temperature (325 °C) sintering using CeO_2 or MnO_2 pastes.

Keywords: organolead Perovskite; low temperature sintering; mesoporous scaffold; oxidation catalyst

1. Introduction

Scaling solar cell manufacturing requires a switch from batch to roll-to-roll (R2R) processing to accelerate throughput [1]. Third generation photovoltaics, such as perovskite solar cells (PSC), offer the potential of R2R manufacturing because these are solution processable and are, therefore, printable devices [2]. However, R2R processing requires flexible substrates; e.g., metal foil or transparent conducting oxide (TCO) coated plastic film. Thus, whilst the most widely used form of TCO-coated glass (fluoride-doped tin oxide—FTO) can withstand 500 °C, these substrates are rigid. By comparison, whilst metal foils are flexible, they rapidly oxidize at this temperature, whilst plastic films (e.g., PET) are limited to ca. 120 °C when under tension, which is necessary for R2R operation. As such, there is a need to lower the manufacturing temperature of perovskite solar cell devices.

A key reason for the global interest in PSC devices is the rapid increase in device efficiencies, leading to a certified world record power conversion efficiency (PCE) of 25.2% [3]. The highest efficiency devices are fabricated using a mesoporous metal oxide scaffold sintered at high temperature >500 °C [4,5]. However, for lower temperature processing (<200 °C), the highest PCE reported for mesoporous metal oxide PSCs is 18.2% [6]. By comparison, low temperature fabrication of non-scaffold PSCs i.e., planar devices, has resulted in PCE >20% [7,8]. Not only does lower temperature processing broaden the range of substrates available to include lower cost substrates, but it also lowers PSC embodied energy [6,9].

For mesoporous PSCs the metal oxide is deposited from a paste containing solvent and organic binders to control the rheology and film morphology before and after deposition [4,5]. High temperature processing is required to burn off the organic binders and sinter the metal oxide particles together [10,11]. Schulze et al. and Brown et al. removed the organic binders while using UV treatment [6,9]. However, our previous work focused on dye sensitized solar cell (DSC) devices, we reported lower temperature binder removal during device fabrication by mixing a metal peroxide oxidation catalyst into a TiO_2 working electrode precursor paste [11]. Here, we have further explored the use of oxidation catalysts by fabricating PSCs while using CeO_2 and MnO_2 mesoporous scaffolds. CeO_2 is well established as an oxidation catalyst, as is discussed in several review articles [12,13]. It has also been reported as an ETL for planar PSCs fabricated at low temperature [14,15]. Xie and Deng et al. reported a PCE of 14.3% for n-i-p PSCs while using a CeO_2 ETL that was deposited from a sol-gel precursor and sintered at 150°C. The PCE was increased to 17.0% by adding an organic ETL as an interlayer between the CeO_2 and perovskite to reduce trap assisted recombination at the interface [14]. Chen et al. reported a champion PCE of 17.0% for p-i-n PSC devices that were fabricated while using CeO_2 as an ETL sintered at 100°C. In their work, the authors state that the CeO_2 ETL is more compact and it offers better moisture resistance in comparison to organic ETLs. PSC devices fabricated while using CeO_2 have also been reported to exhibit improved stability in comparison to devices that were fabricated with an organic ETL [15]. MnO_2 is also a well-established oxidation catalyst [16,17]. To the best of our knowledge, the use of narrow band gap metal oxides, including MnO_2, as ETLs in PSC devices has not been reported before. For n-i-p devices, the reason being is thought to be that a low band gap ETL might absorb photons that would decrease the photocurrent generated by the perovskite absorber. However, MnO_2 has been used to improve the performance of photovoltaic devices. Lee et al. reported enhanced electron injection and decreased recombination in organic light emitting diodes while using MnO_2 as an interlayer between the organic emitter and cathode [18]. Improved electron transport was also reported for DSC devices that were fabricated while using TiO_2-MnO_2 composite working electrodes [19]. MnO_2 has also been reported as a low-cost counter electrode in DSC devices [20].

In this paper, we report the fabrication of methylamine lead tribromide PSC devices using either MnO_2 or CeO_2 mesoporous scaffold layers, which have been compared with mesoporous TiO_2 scaffold devices. The thermal chemistry of the sintering process has been correlated with device data to show the importance of effective sintering to ensure complete binder removal and achieve stoichiometric metal oxide formation to achieve good device efficiencies. The world record device efficiency that is reported for this perovskite absorber is 10.4% [21].

2. Materials and Methods

The materials were purchased from the following suppliers. TiO_2 electron transport layer, Solaronix BL/SC, and FTO (10 Ω per square) substrates were purchased from Solaronix (Aubonne, Switzerland). TiO_2 mesoporous scaffold paste, DSL18NR-T was purchased from Dyesol (Elanora, Australia). MnO_2, CeO_2, terpineol, and ethyl cellulose (48.0–49.5% (w/w) ethoxyl basis) were purchased from Sigma Aldrich (Dorset, UK). Methyl ammonium bromide (CH_3NH_3Br) was purchased from Sigma Aldrich (Dorset, UK) and lead bromide ($PbBr_2$ 99.99%) was purchased from TCI Chemicals (Oxford, UK). The poly-3-hexylthiophene (P3HT) hole transport material (HTM) Mw = 54,200 was purchased from Ossila (Sheffield, UK). Bis(trifluoromethane) sulfonimide lithium salt (LiTFSI) and tertiary butyl pyridine (*t*BP) were purchased from Sigma Aldrich. The anhydrous solvents, including dimethylformamide (DMF), dimethylsulfoxide (DMSO), acetonitrile (CH_3CN), chlorobenzene (ClBz), ethyl acetate (EtOAc), and ethanol (EtOH), were purchased from Sigma Aldrich (Dorset, UK). The solvents for cleaning and rinsing electrodes, including acetone and methanol (MeOH), were purchased from Fisher-Scientific (Loughborough, UK).

CeO_2 and MnO_2 mesoporous scaffold pastes were prepared by adding 0.1 g of ethyl cellulose to 0.8 g of terpineol and stirring until the mixture appeared to be transparent (typical stirring times were

4 h at 800 rpm). To this mixture, 0.1 g of either CeO_2 or MnO_2 was added in *ca.* 0.025 g aliquots with 30 min stirring between additions to minimize metal oxide aggregation.

For control devices, a solution of Solaronix BL/SC (100 μL) was spin coated onto pre-etched, acetone rinsed, and O_2 plasma cleaned FTO substrates (2 cm × 2 cm) at 5000 rpm spin rate for 30 s while using an acceleration rate of 2000 rpm. This TiO_2 layer was heated at 50 °C/min^{-1} to 550 °C and held for 1h. A 150 μL solution of DSL18NR-T mixed with EtOH (1:3 v/v) was spin coated onto this at 2000 rpm spin rate for 30 s using an acceleration rate of 500 rpm. This was heated at 10 °C/min^{-1} to 150 °C, 275 °C, 325 °C, and 450 °C (15 min dwell at each temperature), and finally sintered at 550 °C for 30 min to produce a mesoporous TiO_2 film on an FTO substrate. For CeO_2 and MnO_2 PSC devices, the CeO_2 and MnO_2 pastes were mixed with EtOH (1:3 v/v) and processed as described for TiO_2. However, for low temperature devices, the mesoporous films were heated at 10 °C/min^{-1} to 150 °C, 275 °C, 325 °C (15 min dwell at each temperature) and finally sintered at 325 °C for 30 min.

Methylamine lead tribromide ($CH_3NH_3PbBr_3$) perovskite absorber layers were prepared by mixing $PbBr_2$ (1 g, 2.7 mM) with methylamine bromide (CH_3NH_3Br, 0.31 g, 2.7 mM) in anhydrous DMF (1.6 mL) and anhydrous DMSO (0.4 mL) for 4 h under N_2 to create a perovskite precursor solution. This precursor solution was filtered through a 0.45 μm polytetrafluoroethylene (PTFE) filter (Sigma Aldrich, Dorset, UK) in ambient conditions. 100 μL of $CH_3NH_3PbBr_3$ precursor solution was syringed onto a 2 cm × 2 cm the mesoporous film that had been pre-sintered on a FTO glass substrate. Perovskite films were formed by spin coating by ramping the spin coater to 1000 rpm (ramp rate 500 rpm) for 10 s, followed by a further 30 s at 4000 rpm (ramp rate 2000 rpm). During the final 5 s, 200 μL of anhydrous ethyl acetate was injected onto the sample, resulting in precipitation of the yellow $CH_3NH_3PbBr_3$ perovskite. The films were annealed at 100 °C for 10 min in ambient conditions. The hole transport material (HTM) solution was P3HT (10 mg mL^{-1}) in anhydrous chlorobenzene containing LiTFSI, where 10 μL of a stock solution was prepared while using 0.520 g of LiTFSI in 1 mL anhydrous CH_3CN and *t*BP (10 μL). The HTM solution was gently heated to fully dissolve the components before filtering through a 0.45μm PTFE filter. 100 μL of HTM solution was deposited onto the annealed perovskite and then spin coated at 4000 rpm for 30s (ramp rate 2000rpm). The gold electrodes (ca. 80 nm) were thermally evaporated under vacuum of ~5 × 10^{-6} Torr at a rate of ~ 1 Å s^{-1}.

Current density–voltage (*J-V*) curves for all devices were measured while using a 2400 Series Source Meter (Keithley Instruments, Farnell, Leeds, UK) under simulated AM 1.5 sunlight at 100mW cm^{-2} irradiance using an Abet Class AAB simulator (Sun 2000, Connecticut, US) that was calibrated with a ReRa solutions Si reference cell and with a PSC device active area of 0.15 cm^2. X-ray diffraction data were measured using a Philips Bruker D8 (Cambridge, UK) discover instrument with a Cu source (λ = 1.54060 Å). Thermal gravimetric analysis and differential scanning calorimetry data were measured while using a LABSYS evo STA (Stockport, UK). The pastes were pre-dried at 100–110 °C for 2 h to evaporate the solvent to focus analysis on binder combustion. The samples were ramped at 10 °C min^{-1} under flowing air. The scanning electron microscopy images were measured using a Zeiss Evo MA25 (Cambridge, UK) high resolution scanning electron microscope with a LaB_6 electron source (Cambridge, UK).

To test perovskite stability, the $CH_3NH_3PbBr_3$ films were deposited onto TiO_2, CeO_2, or MnO_2 films, as described previously, these films were then subjected them to UV light (λ = 365 nm) for 24 h using a 6 Watt lamp (Analytikjena UVLS-26 EL Series, Jena, Germany), whilst also in a high humidity environment (>70%). Humidity was generated while using a GenRH Humidity generator (Surface Measurement Systems Ltd., Middlesex, UK) using de-ionized water. X-ray diffraction data of these films were analyzed before and after exposure to UV/humidity.

3. Results and Discussion

3.1. Material Characterization

Figure 1 shows TGA/DSC data for the residue of CeO_2 and MnO_2 pastes after solvent evaporation to focus on the key process of organic binder removal [10,11]. For CeO_2, the majority of mass loss is complete by ca. 350 °C, after which the mass residue remains constant. The major mass loss from 250–350 °C is also associated with a strong exotherm (ca. 310 °C), being in line with a combustion process releasing $CO_{2(g)}$ and heat, respectively. By comparison, the data for the MnO_2 paste show a single mass loss from 175–275 °C. Again, this is associated with a strong exotherm in line with combustion taking place, but this feature is shifted to lower temperature (ca. 260 °C). However, very interestingly, after the combustion event, there is a small weight gain (ca. 3%) as the temperature is increased above 400 °C. We ascribe this to changes in the oxidation state of manganese ions within this metal oxide. Thus, during combustion, O_2 from the surrounding air atmosphere will be consumed to convert the ethyl cellulose binder into $CO_{2(g)}$. At the same time, at these elevated temperatures, it is likely that oxide ions from the MnO_2 particles will be converted into O_2 molecules by the simultaneous reduction of Mn^{4+} ions to Mn^{2+}. However, the mass loss that is associated with this process will be coincident with the ethyl cellulose combustion and so is not resolvable in these TGA data. However, after ethyl cellulose, combustion is complete (ca. 275 °C), the Mn^{2+} ions will be re-oxidized by the additional O_2 molecules present in the flowing air atmosphere. However, because there are no other thermal processes taking place at this point, the uptake of oxygen is observable as a mass increase in the TGA data. This has important consequences for perovskite devices made using MnO_2 films that were sintered at different temperatures, because the presence of Mn^{2+} ions within the lattice will introduce new energy levels that can interfere with efficient device operation.
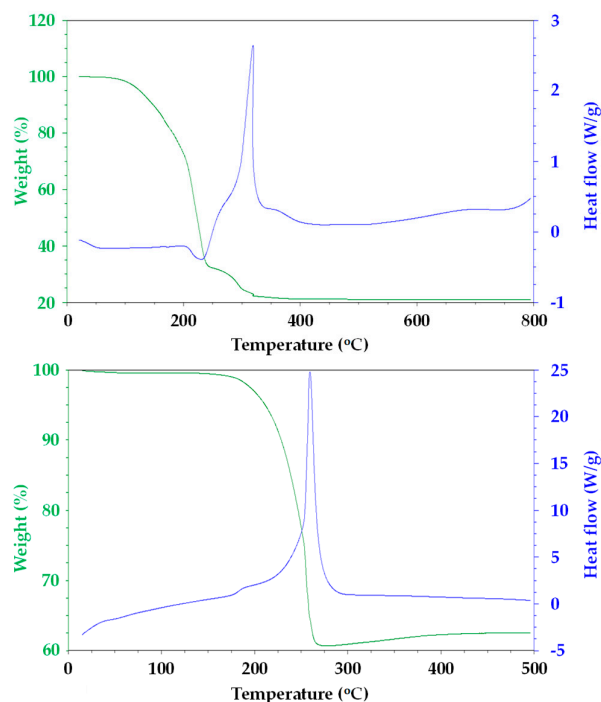

Figure 1. Thermal gravimetric and heat flow data from (top) CeO_2 and (bottom) MnO_2 pastes. Exotherm is up on the heat flow data.

Figure 2 shows X-ray powder diffraction data for sintered, mesoporous metal oxide films. The data have been correlated with standard XRD patterns and they confirm the presence of cassiterite (SnO_2-FTO JCPDS 00-001-0625 and 00-001-0657) in all samples. This is ascribed to the transparent conducting oxide (fluoride-doped tin oxide) that is present on the TEC glass used as the substrate for these metal oxide

films. The data for the ceria film also confirm the presence of crystalline CeO_2 particles (CeO_2-JCPDS 00-001-0800 and JCPDS 00-034-0394). The data are also similar to the raw CeO_2 powder, which suggests that the particles are randomly arranged within the mesoporous film and they do not show preferred orientation. By comparison, the data for the manganese oxide film confirm the presence of crystalline α-MnO_2 particles [22]. Here, again there is no evidence for preferred orientation, which suggests that the MnO_2 particles are randomly arranged in the mesoporous film.
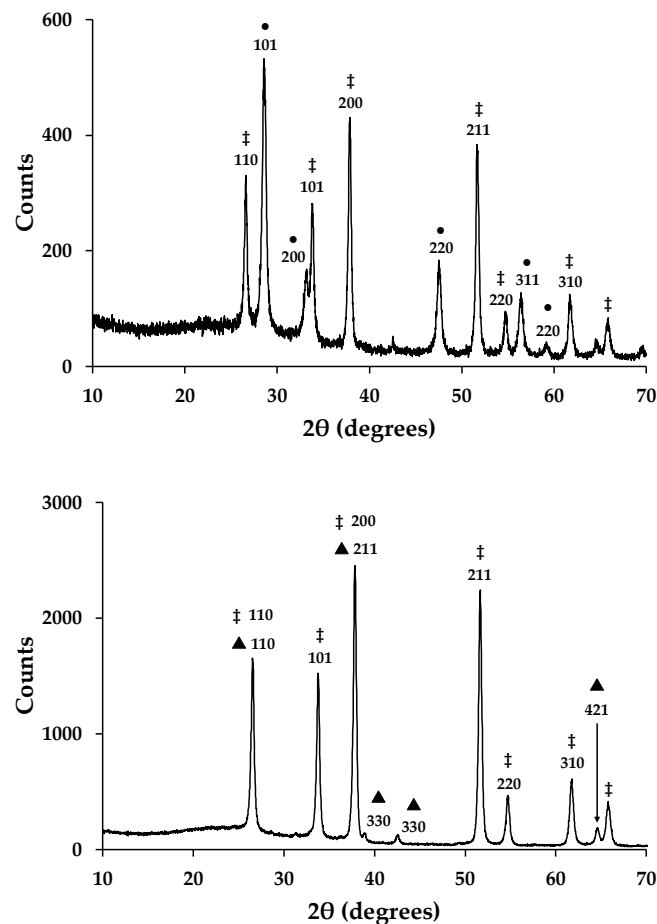

Figure 2. X-ray powder diffraction data for mesoporous films of (top) CeO_2 and (bottom) MnO_2 showing indexed diffraction peaks. Key: ‡ = SnO_2, • = CeO_2, and ▲ = MnO_2.

Figure 3 shows plan view, scanning electron micrographs of CeO_2 and MnO_2 mesoporous films that were sintered at 550 °C. For the majority of the both films, the data show coherent surface coverage. However, both of the films also show larger particulates within the films which suggests that there were larger agglomerates present within the metal oxide pastes deposited onto the substrates. These larger particles would be expected to exert localized changes in device performance, although only over very small surface areas (< 10 μm). The SEM data also suggest that larger particles are present in the MnO_2 film as compared to the CeO_2 film. In parallel with this, the SEM data also suggest that the MnO_2 film is more porous than the CeO_2. In this context, when making repeat batches of metal oxide pastes, we did experience problems of reproducibility from batch to batch of devices, which results from the need to disperse pre-made MnO_2 and CeO_2 powders into solvent with the ethyl cellulose binder. To overcome this required significant mixing and homogenization to ensure consistency. For the majority of the surface, SEM analysis shows that the 550 °C-sintered CeO_2 electrodes show more coherent surface coverage than those sintered at 325 °C. For MnO_2 electrodes, the SEM analysis shows almost identical surface coverage for films that were sintered at 325 °C and 550 °C.
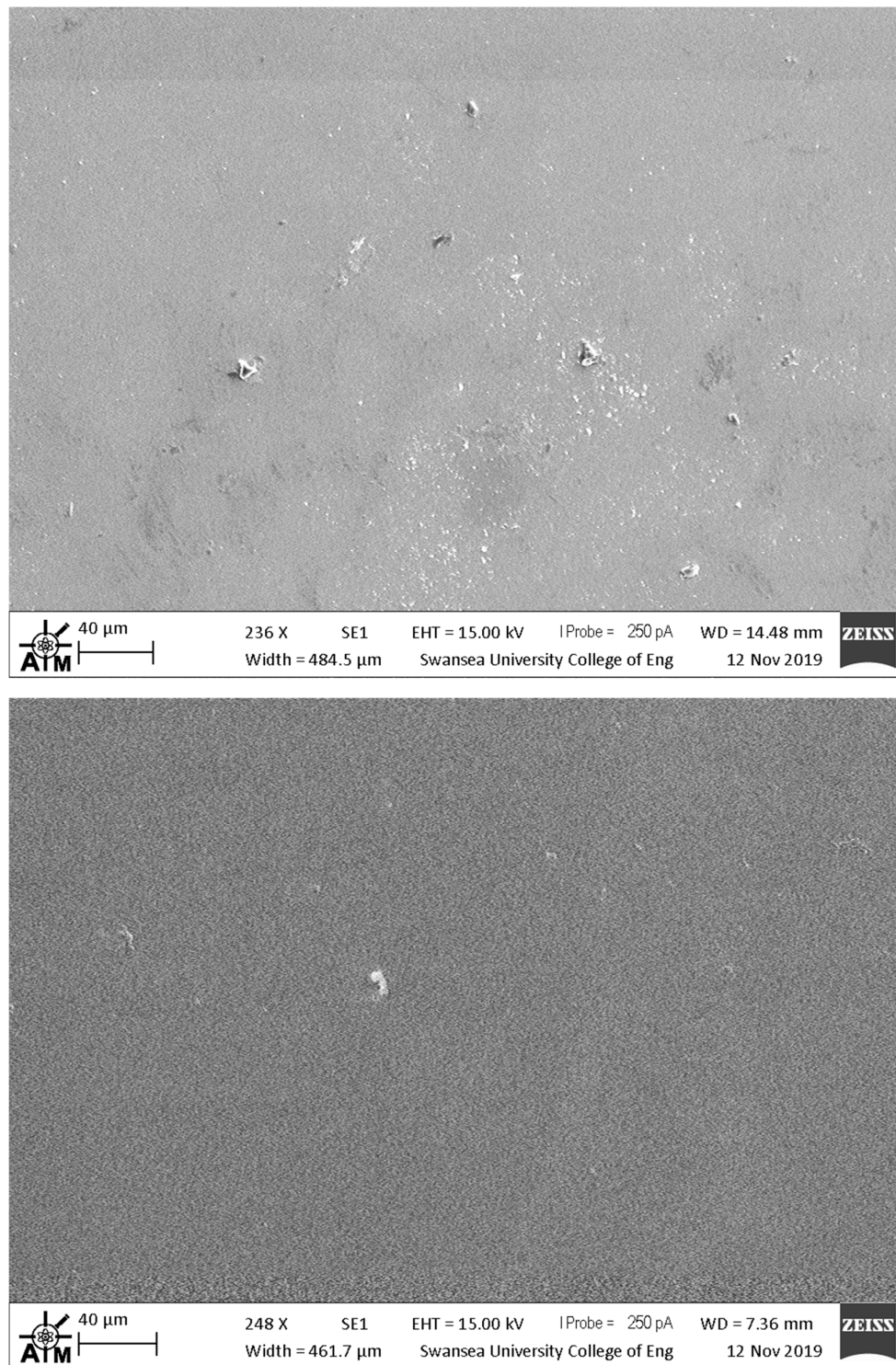
| 40 µm | 236 X | SE1 | EHT = 15.00 kV | I Probe = 250 pA | WD = 14.48 mm | ZEISS |
| | Width = 484.5 µm | | Swansea University College of Eng | | 12 Nov 2019 | |

| 40 µm | 248 X | SE1 | EHT = 15.00 kV | I Probe = 250 pA | WD = 7.36 mm | ZEISS |
| | Width = 461.7 µm | | Swansea University College of Eng | | 12 Nov 2019 | |

Figure 3. SEM images of mesoporous films of (top) CeO_2 and (bottom) MnO_2 films that were sintered at 550 °C on fluoride-doped tin oxide (FTO) glass.

3.2. Perovskite Device Performance

Table 1 and Figure 4 show a summary of the I-V data that were measured for champion devices fabricated during this study. The lowest overall device efficiency ($\eta \approx 0.8\%$) was measured for devices that were fabricated while using CeO_2 as a mesoporous scaffold mainly as a result of poor photocurrent generation ($J_{sc} \approx 2.7$ mA cm^{-2}). By comparison, the MnO_2 PSC device showed a very similar PCE

to the TiO_2 control devices (ca. 3.8%). However, the data show a very substantial (ca. 400 mV) increase in open circuit voltage (V_{oc} = 1.34 V for MnO_2 versus 0.95 V for TiO_2). This was counteracted by lower photocurrent and FF for the MnO_2 devices resulting in a similar overall device efficiency. In addition, the PCE for all devices was higher when measured from open circuit to short circuit. This type of hysteresis is routinely observed for perovskite solar cell devices and is mainly due here to a decrease of V_{oc} and J_{sc} when scanning from short circuit to open circuit (Figure 4). Using these I-V curve data, the hysteresis for TiO_2, CeO_2 and MnO_2 devices has been calculated to be 25.6%, 8.8% and 32.4%, respectively. However, when considering the lower hysteresis that was observed for the CeO_2 devices, it should be noted that the overall PCE for these devices is ca. 80% lower than for the TiO_2 or MnO_2 devices.

Table 1. I-V data for $CH_3NH_3PbBr_3$ PSC devices with mesoporous films sintered at 550 °C. The direction of voltage sweep is shown as oc-sc = open circuit to short circuit and vice versa.

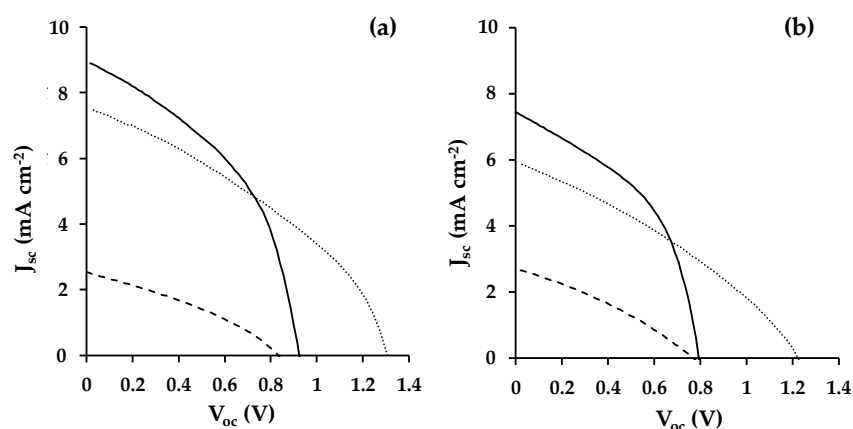| Sample	PCE (%)	V_{oc} (V)	J_{sc} (mA cm^{-2})	FF
TiO_2 oc-sc	3.8	0.95	8.91	0.45
TiO_2 sc-oc	2.9	0.81	7.45	0.47
CeO_2 oc-sc	0.9	0.91	2.55	0.37
CeO_2 sc-oc	0.8	0.87	2.67	0.34
MnO_2 oc-sc	3.9	1.34	7.50	0.38
MnO_2 sc-oc	2.6	1.26	5.89	0.35

Figure 4. PSC I-V data scanned from (**a**) open circuit to short circuit and (**b**) short circuit to open circuit fabricated using metal oxide scaffolds consisting of TiO_2 (solid line), CeO_2 (dashed line), or MnO_2 (dotted line).

Figure 5 shows the variation of device efficiency, V_{oc}, normalized J_{sc}, and fill factor obtained from open circuit to short circuit I-V scans for champion pixels measured from four replicate devices for each metal oxide scaffold type. The data show that the device efficiency and V_{oc} distribution are slightly greater for devices fabricated with MnO_2 scaffolds when compared with TiO_2-based devices. However, the J_{sc} and FF distribution showed the opposite trend with slightly great variation for TiO_2 devices over MnO_2. One explanation for these differences could be that the $CH_3NH_3PbBr_3$ absorber might behave differently between the TiO_2 and MnO_2 devices. Thus, for TiO_2, because the perovskite injects excited state electrons into the TiO_2 scaffold, device efficiency is likely to be most affected by the perovskite-TiO_2 interface and J_{sc} varies the most, because perovskite deposition and surface coverage is likely to be the biggest variable during device manufacture. However, for the MnO_2 devices, there is such an offset in metal oxide/perovskite energy levels (Figure 6), it is unlikely that electron injection into the MnO_2 occurs. Instead, the charge is most likely carried within the perovskite absorber itself, as was first reported by Snaith et al. for electrically insulating Al_2O_3-based perovskite devices [23].

By comparison, with the exception of V_{oc}, the CeO$_2$ devices gave less variable data, but that reflects the consistently poor CeO$_2$ device performance.
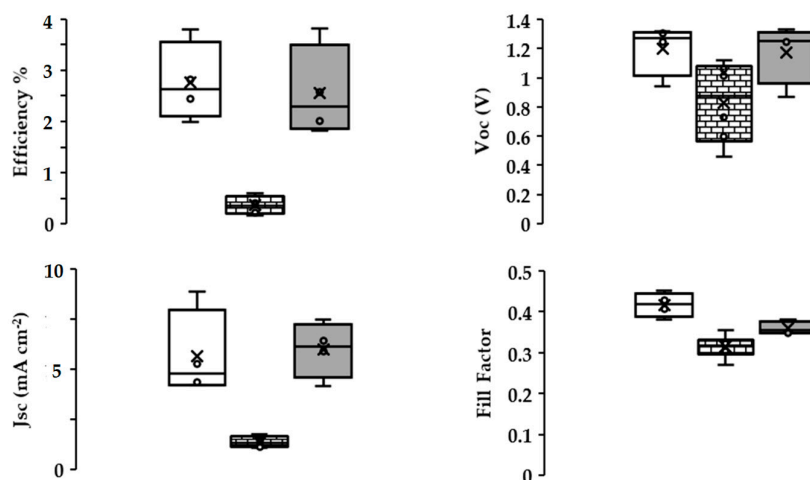

Figure 5. Box plots of (top left) device efficiency, (top right) V_{oc}, (bottom left) normalized J_{sc} and (bottom right) fill factor. TiO$_2$, CeO$_2$, and MnO$_2$ scaffold devices are represented by white, brick and grey fill, respectively. The data for each treatment are from 4 devices each with three pixels representing 12 measurements per sample.
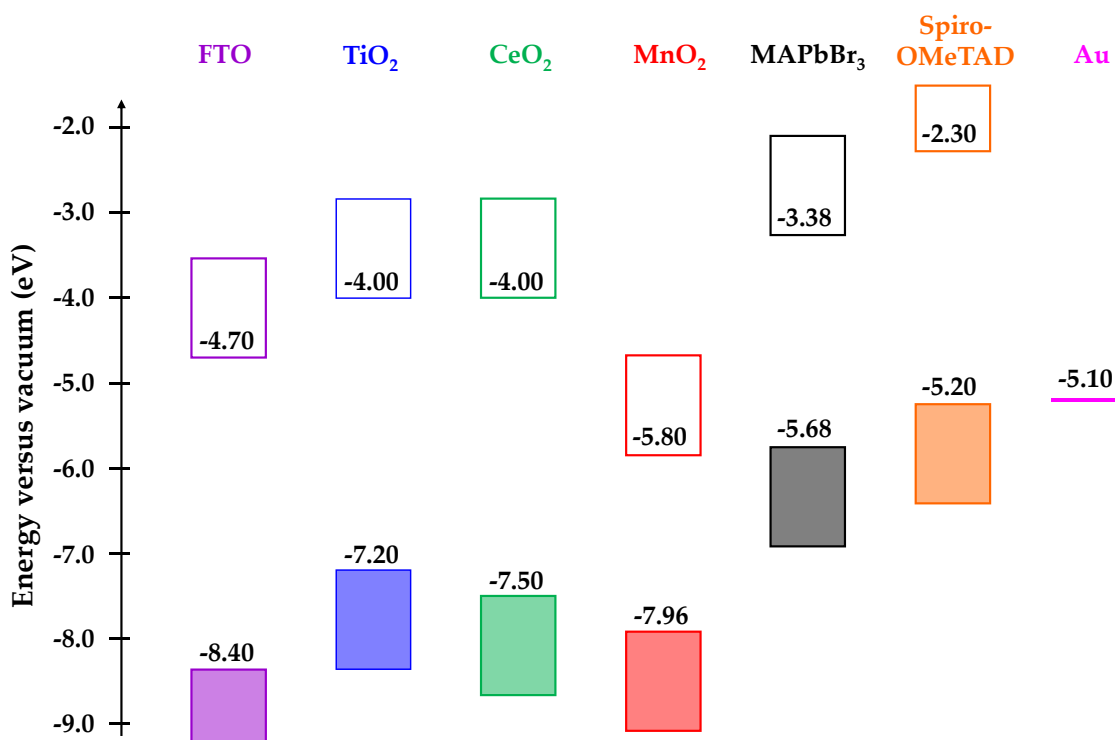

Figure 6. Energy level diagram for TiO$_2$, CeO$_2$, and MnO$_2$ metal oxide scaffolds and CH$_3$NH$_3$PbBr$_3$ (MAPbBr$_3$) perovskite absorber showing conduction bands (clear boxes) and valence bands (shaded boxes). The spiro-OMeTAD hole transport material (HTM) and electrode materials-fluoride-doped tin oxide (FTO) and gold are shown for clarity.

It is important to note that all of the devices were measured through the metal oxide film. Whilst the high band gaps of TiO$_2$ and CeO$_2$ (>3.0 eV) do not, MnO$_2$ has a lower band gap (ca. 2.16 eV), which could absorb light with λ > ca. 570 nm. To study this, we have measured film thickness while using profilometry, which shows that the TiO$_2$ films are 0.40–0.50 μm, the CeO$_2$ films are slightly

thinner (0.15–0.30 µm), whilst the MnO_2 films are the thinnest (0.10–0.15 µm), although they also contain occasional particles up to 0.30 µm, which may act as light scattering particles.

Further analysis of Figure 6 supports these assertions by considering the conduction and valence band energies of the various metal oxide scaffolds and the $CH_3NH_3PbBr_3$ absorber [14,24–26]. Firstly, when comparing TiO_2 and CeO_2, the conduction band edges are in the same place (−4.0 eV). This is 0.62 eV more negative than the conduction band edge of $CH_3NH_3PbBr_3$ and so effective electron injection would be expected into both TiO_2 and CeO_2. The open circuit voltage would also be expected to be similar while assuming similar Fermi levels for both metal oxides and this is what is measured in these devices ($V_{oc} \approx 0.9$ V, Table 1). However, the J_{sc} for TiO_2 is much higher than for CeO_2, which suggests that either there is a poor CeO_2-perovskite interface that limits injection or there are surface trap states on the CeO_2 which recombine with the excited state electrons. Figure 6 also clearly shows the significant energy level mismatch (2.42 eV) between the conduction bands of MnO_2 (−5.80 eV) and $CH_3NH_3PbBr_3$ (−3.38 eV). Such is the offset, the valence band of $CH_3NH_3PbBr_3$ is much closer to the conduction band of MnO_2. As such, electron injection from the $CH_3NH_3PbBr_3$ absorber into the MnO_2 conduction band should result in a decrease of V_{oc} for these devices. However, as discussed previously, the increased V_{oc} that is observed suggests that the MnO_2 is functioning as a scaffold rather than an electron transport layer, as was reported for alumina scaffolds in PSC devices [23].

These assertions are further backed up by the data for devices that were fabricated while using mesoporous scaffolds sintered at lower temperature (325 °C). None of the devices generated any photocurrent, which resulted in device efficiencies of ca. 0%. For CeO_2, although the conduction band edge would be expected to be significantly shifted by a lower sintering temperature, the poor J_{sc} can be explained, because residual carbon would still be expected to be present within the mesoporous films as complete burnout would not be expected until ca. 375 °C (Figure 1). By comparison, for MnO_2 complete carbon burnout would be complete by ca. 275 °C. However, a partial reduction on Mn^{4+} would create reduced manganese ions, which, in turn, would create new defect electronic states in the scaffold. Thus, instead of charge passing through the $CH_3NH_3PbBr_3$, it is assumed that it recombines with these trap states, resulting in zero efficiency devices.

UV-visible spectra have been measured to study the light harvesting of the perovskite-metal oxide films. As such, Figure S1 shows absorbance spectra for $CH_3NH_3PbBr_3$ films that were deposited onto FTO-coated glass coated either with TiO_2, CeO_2 or MnO_2 scaffolds. Each spectrum shows three key features; an absorption edge (I), a peak around 550 nm and a shoulder around 600 nm for the tribromide perovskite. For the TiO_2 sample, the absorption edge is at 350 nm with peaks II and III at 544 nm (2.28 eV) and 601 nm (2.07 eV), respectively. For the CeO_2 sample, these features shift to I = 335 nm, II = 549 nm (2.26 eV), and III = 613 nm (2.03 eV). For the MnO_2 sample, the features are at I = 328 nm, II = 547 nm (2.27 eV), and III = 609 nm (2.04 eV). The data suggest that the MnO_2 layer is sufficiently transparent that it does not limit light harvesting relative to the TiO_2 or CeO_2 scaffolds. We have also run ATR-infrared spectroscopy to confirm the absence of organic residues on the sintered metal oxide scaffolds (Figure S2).

The potential influence of the metal oxide on perovskite crystallisation has also been studied using X-ray diffraction. The data (Figure 7a) show diffraction peaks for the 100, 110, 111, 200, 210, 211, 220, 300, 311, 222, 320, 321, 400, 410, and 411 planes of $CH_3NH_3PbBr_3$ perovskite phase. In all of the samples, the preferred orientation is observed along the 100 and 200 planes. However, for the "as prepared" films, the intensities of the diffraction peaks that were observed for the 111, 210, 211, 220, 300, 311, 222, 320, 321, 400, 410, and 411 planes are higher relative to the 100 and 200 planes for $CH_3NH_3PbBr_3$ material deposited on TiO_2 when compared to the perovskite that was deposited on either CeO_2 (Figure S3) or MnO_2 (Figure S4). This suggests that the preferred orientation is less pronounced for the perovskite that was deposited on TiO_2 when compared to CeO_2 or MnO_2.
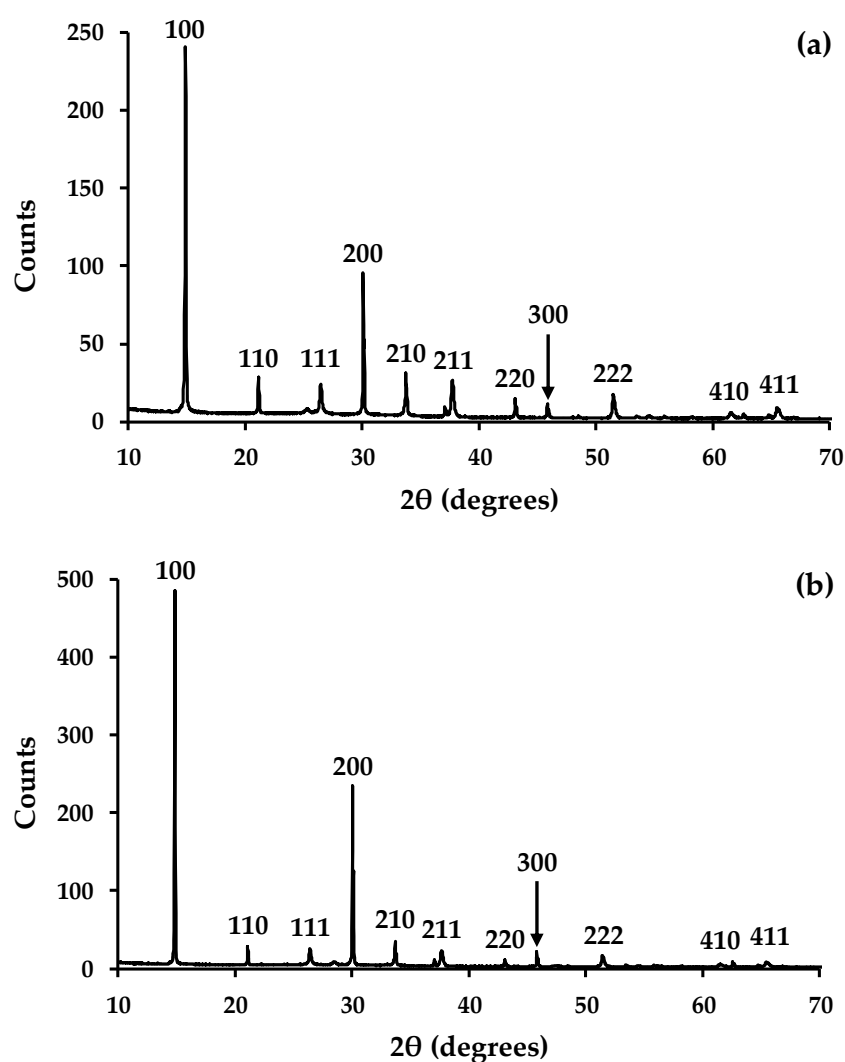
Figure 7. X-ray diffraction data of CH3NH3PbBr3 deposited on a TiO_2 scaffold layer (**a**) as made and (**b**) after 24 h exposure to UV light and 70% relative humidity.

The films were also exposed to a combination of UV light and relative humidity for 24 h to study perovskite stability on the different metal oxide scaffolds. Over this time period, the XRD data show for the $CH_3NH_3PbBr_3$ films deposited on either CeO_2 (Figure S3) or MnO_2 (Figure S4) show that these materials do not change under these conditions. By comparison, the data for $CH_3NH_3PbBr_3$ on TiO_2 (Figure 7b) show a slight increase in the preferred orientation along the 100 and 200 planes, but no evidence for any degradation of the perovskite. We have further tested film stability by exposing all of the films to ambient conditions for a further week and the XRD data (Figure S5) also show no changes to the $CH_3NH_3PbBr_3$ perovskite material. Whilst we have previously observed enhanced perovskite stability for organolead tri-iodide perovskites on alumina scaffolds [27], we ascribe this film stability to the inherently chemical stability of tribromide perovskites. However, these data do suggest that the different metal oxide scaffolds do not have a negative effect on film stability.

4. Conclusions

From a materials perspective, this paper shows that producing mesoporous metal oxide scaffolds while using lower sintering temperatures is possible using CeO_2 or MnO_2. However, residual carbon in CeO_2 or new energy levels created from reduction of Mn^{4+} in MnO_2 do limit solar cell efficiency. However, importantly, the data do suggest that, if energy level mismatches are sufficient, organolead perovskites can still work efficiently with low band gap metal oxides, such as MnO_2, in a similar

manner to the way they operate with large band gap insulators, such as Al_2O_3. Stability data suggest that different metal oxide scaffolds do not limit the inherent chemical stability of organolead tribromide perovskites. This opens up the possibility that it might be possible to use a much wider range of metal oxides as mesoporous scaffolds for perovskite solar cells than previously thought to be possible.

Supplementary Materials: The following are available online at http://www.mdpi.com/1996-1944/13/4/949/s1, Figure S1: UV-visible spectra of $CH_3NH_3PbBr_3$ perovskite films deposited onto (a) TiO_2 scaffold, (b) CeO_2 scaffold, and (c) MnO_2 scaffold, Figure S2: ATR-infrared spectra of 500 °C sintered films of (a) TiO_2 scaffold, (b) CeO_2 scaffold, and (c) MnO_2 scaffold, Figure S3: XRD data of $CH_3NH_3PbBr_3$ films deposited on CeO_2 scaffold; (top) as deposited and (bottom) after 24h exposed to UV and 70% relative humidity, Figure S4: XRD data of $CH_3NH_3PbBr_3$ films deposited on MnO_2 scaffold; (top) as deposited and (bottom) after 24h exposed to UV and 70% relative humidity, Figure S5: XRD data of $CH_3NH_3PbBr_3$ films deposited on (top) TiO_2 scaffold, (middle) CeO_2 scaffold, and (bottom) MnO_2 scaffold after exposure to ambient conditions for 1 week.

Author Contributions: Individual contributions include: conceptualization, P.J.H. and A.C.; film characterization and device making, A.C. and E.W.J.; SEM, UV-vis and ATR-IR, C.P.K.; supervision and funding acquisition, P.J.H. All authors have read and agreed to the published version of the manuscript.

Conflicts of Interest: The authors declare no conflict of interest.

References

1. Holliman, P.J.; Davies, M.L.; Connell, A.; Carnie, M.J.; Watson, T.M. Rapid, low temperature processing of dye sensitized solar cells. In *Functional Materials for Energy Applications*; Kilner, J.A., Skinner, S.J., Irvine, S.J.C., Edwards, P.P., Eds.; Woodhead Publ.: Cambridge, UK, 2012.

2. Holliman, P.J.; Connell, A.; Jones, E.W.; Ghosh, S.; Furnell, L.; Hobbs, R.J. Solvent issues during processing and device lifetime for perovskite solar cells. *Mater. Res. Innov.* **2015**, *19*, 508–511. [CrossRef]

3. The National Renewable Energy Laboratory. Available online: https://www.nrel.gov/pv/cell-efficiency.htmL (accessed on 15 January 2020).

4. Yang, W.S.; Park, B.-W.; Jung, E.H.; Jeon, N.J.; Kim, Y.C.; Lee, D.U.; Shin, S.S.; Seo, J.; Kim, E.K.; Noh, J.H.; et al. Iodide management in formamidinium-lead-halide–based perovskite layers for efficient solar cells. *Science* **2017**, *356*, 1376–1379. [CrossRef] [PubMed]

5. Jena, A.K.; Kulkarni, A.; Miyasaka, T. Halide perovskite photovoltaics: Background, status, and future prospects. *Chem. Rev.* **2019**, *119*, 3036–3103. [CrossRef] [PubMed]

6. Schulze, P.S.C.; Bett, A.J.; Winkler, K.; Hinsch, A.; Lee, S.; Mastroianni, S.; Mundt, L.E.; Mundus, M.; Würfel, U.; Glunz, S.W.; et al. Novel low-temperature process for perovskite solar cells with a mesoporous TiO_2 scaffold. *ACS Appl. Mater. Interfaces* **2017**, *9*, 30567–30574. [CrossRef]

7. Tan, H.; Jain, A.; Voznyy, O.; Lan, X.; Arquer, F.P.G.; Fan, J.Z.; Quintero-Bermudez, R.; Yuan, M.; Zhang, B.; Zhao, Y.; et al. Efficient and stable solution-processed planar perovskite solar cells via contact passivation. *Science* **2017**, *355*, 722–726. [CrossRef]

8. Jiang, Q.; Zhang, L.; Wang, H.; Yang, X.; Meng, J.; Liu, H.; Yin, Z.; Wu, J.; Zhang, X.; You, J. Enhanced electron extraction using SnO_2 for high-efficiency planar-structure $HC(NH_2)_2PbI_3$-based perovskite solar cells. *Nat. Energy* **2016**, *2*, 1–7. [CrossRef]

9. Giacomo, F.D.; Zardetto, V.; Lucarelli, G.; Cinà, L.; Carlo, A.D.; Creatore, M.; Brown, T.M. Mesoporous perovskite solar cells and the role of nanoscale compact layers for remarkable all-round high efficiency under both indoor and outdoor illumination. *Nano Energy* **2016**, *30*, 460–469. [CrossRef]

10. Holliman, P.J.; Connell, A.; Davies, M.; Carnie, M.; Bryant, D.; Jones, E.W. Low temperature sintering of aqueous TiO_2 colloids for flexible, co-sensitized dye-sensitized solar cells. *Mater. Lett.* **2019**, *236*, 289–291. [CrossRef]

11. Holliman, P.J.; Muslem, D.K.; Jones, E.W.; Connell, A.; Davies, M.L.; Charbonneau, C.; Carnie, M.J.; Worsley, D.A. Low temperature sintering of binder-containing TiO_2/metal peroxide pastes for dye-sensitized solar cells. *J. Mater. Chem. A* **2014**, *2*, 11134–11143. [CrossRef]

12. Trovarelli, A. Catalytic properties of ceria and CeO_2-containing materials. *Catal. Rev.* **1996**, *38*, 439–520. [CrossRef]

13. Montini, T.; Melchionna, M.; Monai, M.; Fornasiero, P. Fundamentals and catalytic applications of CeO_2-based materials. *Chem. Rev.* **2016**, *116*, 5987–6041. [CrossRef] [PubMed]

14. Wang, X.; Deng, L.-L.; Wang, L.-Y.; Dai, S.-M.; Xing, Z.; Zhan, X.-X.; Lu, X.-Z.; Xie, S.-Y.; Huang, R.-B.; Zheng, L.-S. Cerium oxide standing out as electron transport layer for efficient and stable perovskite solar cells processed in low temperature. *J. Mater. Chem. A* **2017**, *5*, 1706–1712. [CrossRef]

15. Hu, T.; Xiao, S.; Yang, H.; Chen, L.; Chen, Y. Cerium oxide as an efficient electron extraction layer for p–i–n structured perovskite solar cells. *Chem. Commun.* **2018**, *54*, 471–474. [CrossRef] [PubMed]

16. Zhang, S.; Zhang, B.; Liu, B.; Sun, S. A review of Mn-containing oxide catalysts for low temperature selective catalytic reduction of NOx with NH_3: Reaction mechanism and catalyst deactivation. *RSC Adv.* **2017**, *7*, 26226–26242. [CrossRef]

17. Ye, Z.; Giraudon, J.-M.; Geyter, N.D.; Morent, R.; Lamonier, J.-F. The design of MnOx based catalyst in post-plasma catalysis configuration for toluene abatement. *Catalysts* **2018**, *8*, 91. [CrossRef]

18. Lee, H.; Lee, J.; Jeon, P.; Jeong, K.; Yi, Y.; Kim, T.G.; Jeong, W.-K.; Lee, J.W. Highly enhanced electron injection in organic light-emitting diodes with an n-type semiconducting MnO_2 layer. *Org. Elec.* **2012**, *13*, 820–825. [CrossRef]

19. Prasetio, A.; Habieb, A.M.; Alkian, I.; Arifin, Z.; Widiyandari, H. Dye-sensitized solar cell based on TiO_2/MnO_2 composite film as working electrode. *IOP Conf. Series: J. Physics: Conf. Series.* **2017**, *877*, 012005. [CrossRef]

20. Ahmad, K.; Mohammad, A.; Mobin, S.M. Hydrothermally grown α-MnO_2 nanorods as highly efficient low cost counter-electrode material for dye-sensitized solar cells and electrochemical sensing applications. *Electrochim. Acta* **2017**, *252*, 549–557. [CrossRef]

21. Heo, J.H.; Song, D.H.; Im, S.H. Planar $CH_3NH_3PbBr_3$ Hybrid Solar Cells with 10.4% Power Conversion Efficiency, Fabricated by Controlled Crystallization in the Spin-Coating Process. *Adv. Mater.* **2014**, *26*, 8179–8183. [CrossRef]

22. Liu, Q.; Ji, S.; Yang, J.; Wang, H.; Pollet, B.G.; Wang, R. Enhanced cycleability of amorphous MnO_2 by covering on α-MnO_2 needles in an electrochemical capacitor. *Materials* **2017**, *10*, 988. [CrossRef]

23. Lee, M.M.; Teuscher, J.; Miyaska, T.; Murakami, T.N.; Snaith, H.J. Efficient hybrid solar cells based on meso-superstructured organometal halide perovskites. *Science* **2012**, *338*, 643–647. [CrossRef] [PubMed]

24. Mahmood, K.; Sarwar, S.; Mehran, T.M. Current status of electron transport layers in perovskite solar cells: Materials and priorities. *RSC Adv.* **2017**, *7*, 17044–17062. [CrossRef]

25. Xu, Y.; Schoonen, M.A.A. The absolute energy positions of conduction and valence bands of selected semiconducting minerals. *Am. Mineral.* **2000**, *85*, 543–556. [CrossRef]

26. Ansari, M.I.H.; Qurashi, A.; Nazeeruddin, M.K. Frontiers, opportunities and challenges in perovskite solar cells: A critical review. *J. Photochem. Photobiol. C.* **2018**, *35*, 1–24. [CrossRef]

27. Jones, E.W.; Holliman, P.J.; Bowen, L.; Connell, A.; Kershaw, C.; Meza-Rojas, D.E. Hybrid Al_2O_3-$CH_3NH_3PbI_3$ Perovskites towards Avoiding Toxic Solvents. *Materials* **2020**, *13*, 243. [CrossRef] [PubMed]